NRC Publications Archive
Archives des publications du CNRC

Process operational windows and industrialization scenarios for assembly or large aluminium structures by robotic friction stir welding
Wanjara, P.; Monsarrat, B.; Larose, S.

National Research Council Canada   Conseil national de recherches Canada

Canada

Process operational windows and industrialization scenarios for assembly of large aluminium structures by robotic friction stir welding

P. Wanjara, B. Monsarrat, and S. Larose

Abstract. In this work, friction stir welding (FSW) of 3.18 mm thick AA6061-T6 sheets in the butt- and lap-joint configuration was investigated with the objective of industrializing the process using low-cost serial industrial robots. The influence of weld pitch on the welding defects, microstructure, hardness, and bend performance of butt and lap welds was examined to identify process operational windows for both joint types. In parallel with these trials, a methodology based on kinetostatic analysis was developed to identify and evaluate viable robotized scenarios for FSW. On the basis of the experimental FSW process development results, this methodology was then applied to identify optimized FSW scenarios for the fabrication of large integrated AA6061 structural components with stringer-to-skin and skin-to-skin joints. Candidate workcell layouts are also presented.

Résumé. Dans ce travail, le soudage par friction malaxage (mieux connu sous l'acronyme FSW pour Friction Stir Welding) de feuilles d'aluminium 6061-T6 d'une épaisseur de 3.18 mm dans les configurations bout-à-bout et par recouvrement a été étudié dans l'optique d'industrialiser le procédé via l'utilisation de robots sériels industriels à bas coût. L'influence du pas de soudage (weld pitch) sur les défauts de soudage, la microstructure, la dureté et la performance en flexion a été examinée afin d'établir les fenêtres opératoires du procédé pour les deux types de soudure. En parallèle de ces essais expérimentaux, une méthodologie basée sur l'analyse cinétostatique a été développée afin d'identifier et d'évaluer des scénarios viables d'implantation du soudage par friction malaxage robotisé. Cette méthodologie a par la suite été appliquée en utilisant les résultats des tests expérimentaux de soudage afin d'identifier des scénarios d'implantation optimisés pour l'assemblage de composants structurels intégrés de grande dimension en AA60601 comprenant à la fois des joints lisse sur revêtement et revêtement sur revêtement. Des scénarios d'implantation potentiels ont été identifiés et sont présentés.

Introduction

Weight reduction of components and structures utilized in air, land, and marine transportation vehicles is a global challenge facing the manufacturing sector. Aluminium alloys are amongst the most prevalent materials for light weighting of next-generation vehicles with due consideration of their relatively high strength, good workability, and high resistance to corrosion as well as recyclability. Considering the different aluminium alloys, the family of Al-Mg-Si grades, such as aluminum alloy (AA) 6061, plays an important role in the transportation industry. However, when applying conventional fusion welding techniques, butt joints or lap joints, typically encountered in the assembly of long and (or) large structural products, are especially challenging to manufacture without distortion and defects. Aluminium alloys of the 6000 series have high thermal conductivity, high strength, and low weldability; this combination of properties necessitates the

use of special welding procedures to prevent solidification cracking and to minimize residual stresses (Indira Rani et al., 2011; Zhang et al., 2000).

In this respect, friction stir welding (FSW), an emerging solid-state thermo-mechanical joining technology, invented by Wayne Thomas at The Welding Institute (TWI) in 1991 (Thomas et al., 1991), presents a tremendous potential for the assembly of AA6061 structures. As an alternative to conventional fusion welding technologies, FSW is particularly advantageous for the assembly of aluminium alloys due to the low heat input, which is likely to translate into better mechanical performance of the joint and lower welding-induced distortion of the assembly. FSW also has the flexibility to join extruded and rolled materials without requiring complicated surface preparation or shielding gas protection (Khalid Rafi et al., 2010). In friction stir butt welding (FSBW), a cylindrical-shouldered tool with a

P. Wanjara, B. Monsarrat and S. Larose*. Structures, Materials and Manufacturing, National Research Council Canada – Aerospace, Montreal, QC, Canada.

*Corresponding author (e-mail: simon.larose@nrc-cnrc.gc.ca)

profiled pin (threaded, unthreaded, or complicated flute) on its extremity is rotated at a constant advancing speed and plunged at the abutting interface until contact is made between the shoulder and the top surface of the workpieces. By contrast, in friction stir lap welding (FSLW), the rotating tool is plunged through the bottom surface of the top workpiece such that it extends into the bottom workpiece. In either case, a downward forging force is applied during FSW to generate sufficient localized heat and induce plasticization and material movement within a volumetric region surrounding the tool (Fersini and Pirondi, 2008; Threadgill et al., 2009). The heat is generated from friction between the faying surfaces of the tool shoulder and pin against the workpiece as well as adiabatic heating due to plastic straining of the material near the pin at high strain rates. In this way, the material surrounding the tool is softened without reaching the melting point. The rotating and translating movements of the tool during welding result in material transfer around the periphery of the pin. For a comprehensive description of the FSW process, the interested reader can refer to Mishra and Ma (2005).

Development and optimization for FSW involve varying the different tool geometries and process parameters to interrelate the microstructure and performance characteristics. Hence, for both butt and lap welds an operating process window can be defined that identifies conditions under which the risk of defects can be mitigated and (or) eliminated. Of the two joint configurations, the lap type is considered to be more difficult to weld due to the orientation of the interface and the necessity to break the oxide layer on the planar surfaces of the two sheets (Mahoney, 2007). Although tool design can enhance stirring during FSW, a strategic methodology to break the double oxide layer at the advancing side of the weld nugget is to use a double pass process to promote the counter flow of material and eliminate the hooking defect, as suggested by Cederqvist and Reynolds (2000) and further investigated by (Dubourg et al., 2010). In line with this previous methodology, TWI developed a staggered Twin Stir^{TM} variant of the FSW process that is targeted to provide dual stirring of the weld nugget (Scialpi et al., 2006).

In this work, the operational process window for FSW of 3.18 mm thick AA6061-T6 sheets in the butt- and lap-joint configurations was determined with the objective of industrializing the process for the fabrication of large integrated structural components. Recent investigations have demonstrated that heavy payload serial industrial robots offer promising characteristics in terms of workspace and 3-dimensional (3-D) capabilities at a much lower industrialization cost than typical gantry-based FSW systems. Smith and Hinrichs (2006) developed a production-capable FSW system based on a standard industrial robot to achieve friction stir welds in AA6061-T6 with penetrations up to one inch. Voellner et al. (2006) demonstrated the capability and performance of a modified heavy payload KUKA KR500 industrial serial robot for 3-D seam geometries, including highly curved surfaces. Soron and Kalaykov (2006) modified a standard

industrial robot by replacing its sixth axis with FSW-related equipment and proved that such a system could achieve 3-D FSW. However, the lack of stiffness and low payload capabilities limit the advancing speed, plate thickness, and material that can be welded. Specifically during FSW, robot deflections, due the limited robot stiffness, result in tool deviations (such as oscillations and offsetting) from the programmed robot path and, eventually, misalignment from the joint line. Zimmer and Laye (2009) recommended integration of a seam tracking system in the process control architecture to compensate for this limitation, whereas Monsarrat et al. (2009) used model-based real-time compensation of tool deviations based on force sensor measurements to emulate performances of rigid CNC machines for FSW applications. Also, challenges related to the low payload capabilities exist when designing the robotic scenario to ensure that the robotic operational window is compatible with the process conditions. A methodology is thus presented in this paper to address this issue for stringer-to-skin (lap-type joints) and skin-to-skin (butt-type joints) large assemblies.

Experimental procedures

Materials and joining conditions

AA6061 in the T6 temper (solution heat treated and artificially aged) was received in sheet form with a nominal thickness of 3.18 mm and a measured chemical composition of 0.95% Mg, 0.61% Si, 0.32% Cu, 0.3% Fe, and balance aluminium. The average Vickers microhardness (HV) in the as-received condition was 100 ± 4 HV. The as-received microstructure of AA6061-T6 consisted of fully recrystallized grains that were equiaxed in the short-transverse direction and elongated in the longitudinal and transverse directions. Also, second-phase particles (most likely magnesium silicide $\beta'(Mg_2Si)$) were noted along the grain boundaries as well as within the grains. The sheets were sectioned into 400 mm long by 100 mm wide coupons for the FSBW trials and into 200 mm long by 100 mm wide coupons for the FSLW trials. Prior to joining, the edges to be welded were milled (in the case of FSBW trials) and then prepared for welding by degreasing the joint surfaces with ethanol, followed by grinding with a scouring pad to remove the surface oxides, and finally by cleaning in ethanol to remove any surface debris according to ISO standard TR 17671-7 (2004) and also following the general recommendations of AWS specification D17.3/D17.3M:2010. The welding trials were conducted in the direction parallel to the rolling (or L) direction of the material, using a 5-axis MTS ISTIR Process Development System.

The FSW tools were made of H13 steel having a hardness of 46.6–50 HRC (Rockwell C Scale Hardness). Butt welding was investigated using a scroll shoulder tool and a left-hand threaded pin. The shoulder-to-pin diameter ratio was 2.6. The tool-to-workpiece angle was maintained at 0.5° for all welds. To optimize the process, the weld pitch, or ratio of the

advancing speed to the spindle rotation speed, was initially varied from 0.1 to 1.0 mm/rev. Then, for a constant weld pitch within the determined process operating window, various welds were manufactured by varying the advancing speed to identify a set of high productivity rate welding parameters. Lap welding was investigated using a scroll shoulder tool, either a left-hand threaded pin or a right-hand threaded pin and a shoulder-to-pin diameter ratio of 3. Standard double pass welds were performed with the same tools and process parameters for both passes, although the tools were offset towards the advancing side of the first weld for the second pass. Similar to the butt welds, the tool-to-workpiece angle was maintained at $0.5°$ for each lap weld. The weld pitch was varied from 0.07 to 0.31 mm/rev at a constant spindle rotation speed.

Sample preparation and analysis techniques

Weld characteristics such as penetration, weld bead features, and surface quality were first evaluated through visual examination and up to 20 times magnification using a stereomicroscope (Olympus SZX-12). Additionally, metallographic samples of the transverse weld sections were prepared for the selected weld conditions using a precision cut-off saw followed by cold mounting and automated grinding and polishing. Etching with Keller's reagent was used to reveal the general macrostructure of the weldments.

The Vickers microhardness profiles across the selected welds were measured in accordance with ASTM E384 using a Struers Duramin A300 machine equipped with a fully automated testing cycle (stage, load, focus, and measure). Specifically, a test load of 200 g was applied using a load cell with closed-loop circuit control. For each weld condition, three sets of hardness measurements with an indent interval of about 0.2 mm and a dwell period of 15 seconds were performed across the welds, i.e., near the top, middle, and bottom, and the average hardness profile was calculated and reported in this work. It is noteworthy that according to ASTM E384, the spacing between two adjacent indentations must be at least three times the diagonal length of the indentation. Hence, the spacing between two adjacent indentations during microhardness testing was suitably selected to avoid any potential effect of the strain fields caused by adjacent indentations.

For each process condition that was considered, four bend tests were performed after assembly to check the joint integrity. For the butt welds, bend testing was conducted on the basis of CSA W47.2, except for the bend radius that was only 5 mm against a recommended radius of 15 mm, as the former was found to be more sensitive to ductility changes. Additionally, the friction stir butt-joint area, which was comprised of the weld nugget, thermo-mechanically affected zones, and heat affected zones, was centered in relation to the bend radius. In this way, by conducting root and face bend tests on the butt welds, both surfaces of the joint area were placed in tension. By contrast, the lap welds were bent into an S-shape to place the joint area in tension to effectively open any cracks generated by the FSW process. This procedure, referred to as the hammer S-bend test, was carried out with the joint area of the friction stir weld unrestrained (Colegrove et al., 2004; Thomas and Dolby, 2002).

FSW process window investigation for butt-weld configuration

At a constant spindle rotation speed, the effect of increasing the weld pitch on the macrostructural evolution

(a) Poor surface finish

(b) Weld nugget softening

(c) Zigzag oxide layer and wormholes
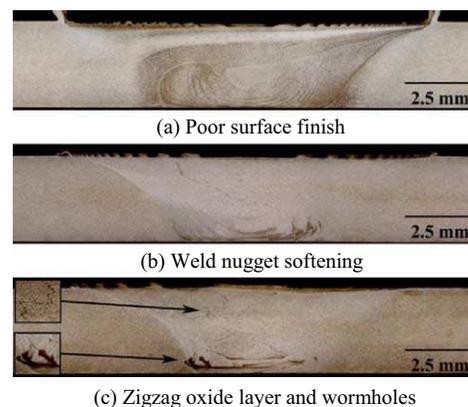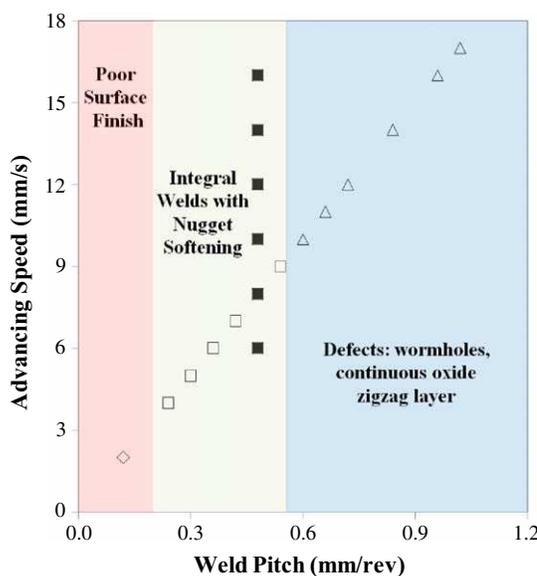
Figure 1. Processing map and typical macrostructures for friction-stir butt welding of AA6061-T6. The open markers represent a series of conditions undertaken at different weld pitch values and the closed markers were conducted at a constant weld pitch value of 0.48.

is illustrated in **Figure 1**. Under hot welding conditions, i.e., using a low weld pitch with a low advancing speed, over-stirring of the weld nugget was observed. Specifically, dark bands were apparent in the weld nugget and the hardness difference of 12 HV measured between these bands and the surrounding regions (Wanjara et al., 2013) could be attributed to local differences in the concentration of Si, Mn, Fe, and Mg (Reddy et al., 2009). These welding conditions also corresponded to heavy material expulsion on the top surface, combined with unacceptable surface finish and plate thinning. Increasing the weld pitch above 0.12 mm/rev resulted in the faint presence of a discontinuous zigzag oxide layer (as revealed in the inset of **Figure 1c**) in the weld nugget, which represents a memory of the joint line, whereas the dark bands in the weld nugget became increasingly diffuse. With further increases in the weld pitch, the zigzag oxide in the weld nugget became more pronounced as it evolved from a discontinuous to a continuous layer with decreasing heat input (i.e., transformation of the process from hot to cold welding conditions). This phenomenon was observed in previous work by Okamura et al. (2002) who reported that below a weld pitch of 0.60 mm/rev, the characteristics of the zigzag oxide are not problematic for the performance of the weld. In the present work, root and face bend testing of joints with different pitch values (**Figure 2**) exhibited no cracking even up to a 180° bend. However, macrostructural observations indicated the formation of wormholes or tunnel defects at the root of the weld on the advancing side at a weld pitch value greater than 0.60 mm/rev. The severity of defects was noted to increase concomitantly with weld pitch. The occurrence of the wormhole running along the weld length on the advancing side of the weld nugget is a consequence of insufficient material transport around the tool pin to the advancing side that results in insufficient consolidation of the plasticized material (Crawford et al., 2006).

Figure 3 illustrates the effect of the weld pitch on the microhardness profile across the welded joints. In general, the microhardness of the weld nugget was lower than the as-received base material (BM), with microhardness in and around the weld center ranging, respectively, from 60.0 HV to 64.9 HV (60.0%–64.9% of BM) for a low weld pitch value of 0.12 mm/rev, from 67.5 HV to 75.8 HV (67.5%–75.8% of BM) for a medium weld pitch of 0.48 mm/rev and from 70.8 HV to 81.5 HV (70.8%–81.5% of BM) for a high weld pitch

value of 0.96 mm/rev. The occurrence of two hardness minima on either side of the weld center was apparent for high weld pitch values, producing an overall W-shape profile that is typical of friction stir welds in precipitation hardened aluminium alloys and may be reasoned through consideration of the influence of the thermal history of the process on the precipitation of strengthening phases. Specifically, heating of the weld nugget and thermo-mechanically affected zones over the solution heat treatment temperature of the alloy completely dissolves the strengthening precipitates, and rapid cooling after FSW gives a super saturated solid solution of alloying elements in the weld nugget (Fratini et al., 2008). Natural aging after welding then gives rise to a slight hardness increase in the weld nugget. In the heat affected zones, the temperatures are sufficient to cause precipitate coarsening and, in this overaged region, softening is clearly evident through the occurrence of a hardness minima at the heat affected – thermo-mechanically affected zone boundary. To this end, the hot welding conditions using a low weld pitch (e.g., 0.12 mm/rev) produced maximal softening, transforming the typical W-shape distribution to almost a U-shape; in contrast, cold welding conditions corresponding to weld pitch values ≥ 0.6 mm/rev resulted in another hardness minimum on the retreating side of the weld nugget due to the occurrence of wormhole and tunnel defects.

In consideration of these microhardness results, a weld pitch value of 0.48 mm/rev appears to allow good weld integrity, i.e., mitigation of wormhole defects and limited softening in the weld nugget for FSW of 3.18 mm thick AA6061-T6. This weld pitch value is in agreement with the threshold of 0.53 mm/rev determined by Liu et al. (1997) for FSW of 5 mm thick AA6061-T6; above 0.53 mm/rev the degradation in weld integrity compromised the mechanical properties of the welded joint. In the present case of 3.18 mm thick AA6061-T6, using a weld pitch value of 0.48 mm/rev, a relatively high joint efficiency (76%) was reported previously by the present authors (Wanjara et al., 2013); in comparison, a lower weld pitch value of 0.2 mm/rev rendered a lower joint efficiency (64%) for FSW of 3 mm thick AA6061-T6 (Moreira et al., 2009). It is noteworthy that joint efficiency refers to the ratio between ultimate tensile strength of the welded joint to that of the BM. As such, a weld pitch value of 0.48 mm/rev was deliberated to be a promising process condition for manufacturing
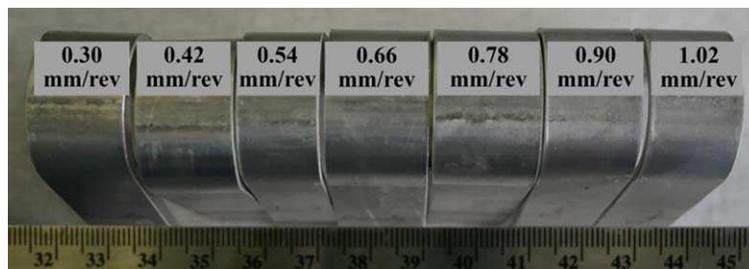

Figure 2. Bend test results for AA6061-T6 friction-stir butt welds joined at different weld pitch values (root face is shown).
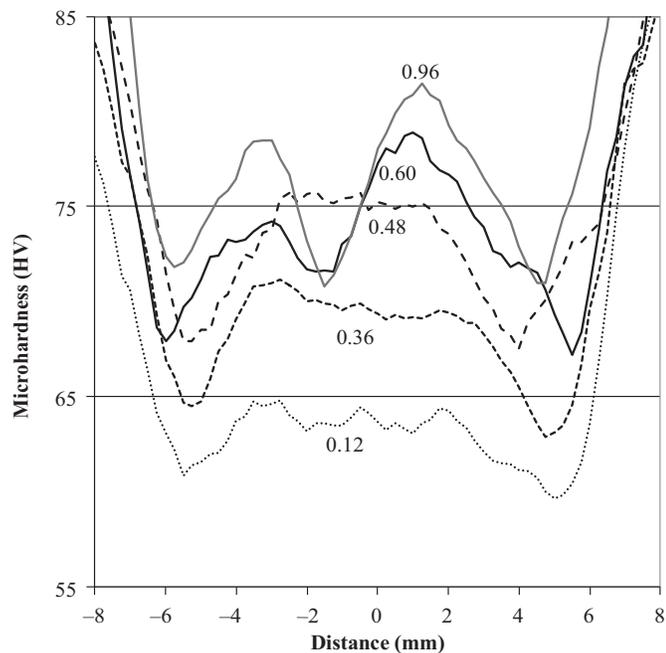
Figure 3. Microhardness evolution in the weld nugget for different weld pitch values. Advancing side is on the right and retreating side on the left.

Figure 4. Forge force variation with increasing weld pitch for friction-stir butt welding of AA6061-T6.

and thus was selected in this work to simulate industrial implementation of the FSW process. Various welds were then produced at this pitch value, as illustrated by the solid black markers in **Figure 1**, using different combinations of advancing speed and rotational speed. Because each test condition was observed to produce a similar macrostructure and to pass bend testing, a condition with high advancing speed was selected to investigate the robotic scenarios, so as to maximize the productivity of the FSW process for industrial applications. Hence, with a view towards industrialization using serial industrial robots, the force amplitudes were recorded during FSW so as to understand the force capability requirements within the process operational window. **Figure 4** provides a record of the forge force as a function of the weld pitch for a constant spindle rotation speed. It can be seen that the forge force increased from 6.72 kN to a maximal value of 10.67 kN at a weld pitch of 1.02 mm/rev, whereas the selected weld pitch of 0.48 mm/rev corresponded to a forge force amplitude of 7.45 kN. Records of the forge force as a function of advancing speed for a weld pitch of 0.48 mm/rev (not presented here) showed little influence of the advancing speed, with an average forge force of 7.30 kN and a standard deviation of 0.21.

FSW process window investigation for lap weld configuration

Figures 5a and **5c** present the macrostructure and the corresponding bend testing results for a friction stir lap weld

performed with a left-hand threaded pin at a high spindle rotation speed and a low weld pitch of 0.10 mm/rev. The double pass welding process adequately fractured the double oxide layer at the sheet interface and produced a well-stirred weld nugget with no cavities. However, the upwards material flow lifted the interface on both the advancing and retreating sides of the weld nugget, causing severe thinning of the top sheet. This defect is apparent in the bend test result as the weld fractured prematurely, following the lifting of the interface. **Figures 5b** and **5d** reveal the macrostructure and the corresponding bend test result for a friction stir lap weld performed under similar conditions but at a higher weld pitch of 0.31 mm/rev. The interface lifting and sheet thinning are still noticeable although less prominent than at 0.10 mm/rev. Additional trials performed using the same weld pitch but for a low rotation speed led to similar results. In addition, for all rotation speeds examined in this work, the welds displayed unacceptable material expulsion.

Interface lifting and top sheet thinning can be explained by the upward material flow produced by the combined effect of a left-hand threaded pin tool and clockwise tool rotation. Therefore, a second set of tools with the same geometrical dimensions but with a right-hand threaded pin configuration was studied to mitigate upward material flow during welding. FSLW using a weld pitch of 0.07–0.27 mm/rev with this new pin configuration was observed to result in acceptable material expulsion, together with a well-formed weld nugget containing no cavities and little or no thinning of the sheet material. Each weld passed bend testing, and a condition with a high weld pitch of 0.27 mm/rev was then selected to
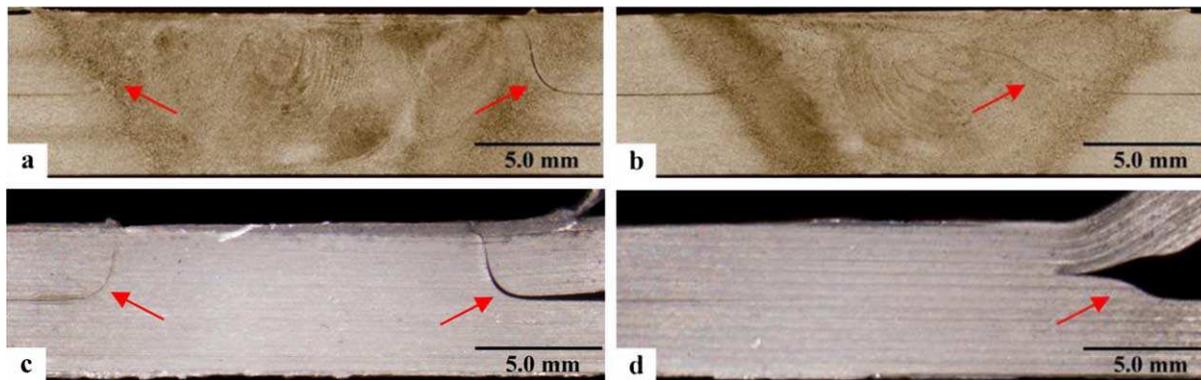
Figure 5. Friction-stir lap welded AA6061-T6, welded with left-hand threaded pin at high spindle rotation speed. Red arrows indicate the lifted interfaces. Macrostructure for weld pitch = 0.10 mm/rev (a); macrostructure for weld pitch = 0.31 mm/rev (b); bend testing for weld pitch = 0.10 mm/rev (c); bend testing for weld pitch = 0.31 mm/rev (d).

conduct FSLW under high productivity conditions. Specifically, **Figures 6a** and **6b** present the macrostructure and the corresponding bend test result for a friction stir lap weld performed at a weld pitch of 0.27 mm/rev. The double-pass welding process produced two well-stirred weld nuggets with no cavities (**Figure 6a**). However, the double oxide layer at the sheet interface was completely fractured only in the overlap area between the two weld nuggets. Slight thinning of the lower sheet was also noticed. Under this process condition, the lap weld passed bend testing (**Figure 6b**) and was

demonstrated to have acceptable Vickers microhardness profiles above and below the sheet interface as shown in **Figure 6c**. It can be noted that the microhardness below the sheet interface is in the same range as in a butt weld performed at a similar weld pitch (see **Figure 3**), whereas the values are slightly larger above the interface. **Figure 7** shows that the forge force during lap welding generally increased with weld pitch. For the process conditions studied in this work, a maximum forge force of 11.9 kN was recorded, corresponding to a weld pitch of 0.27 mm/rev.
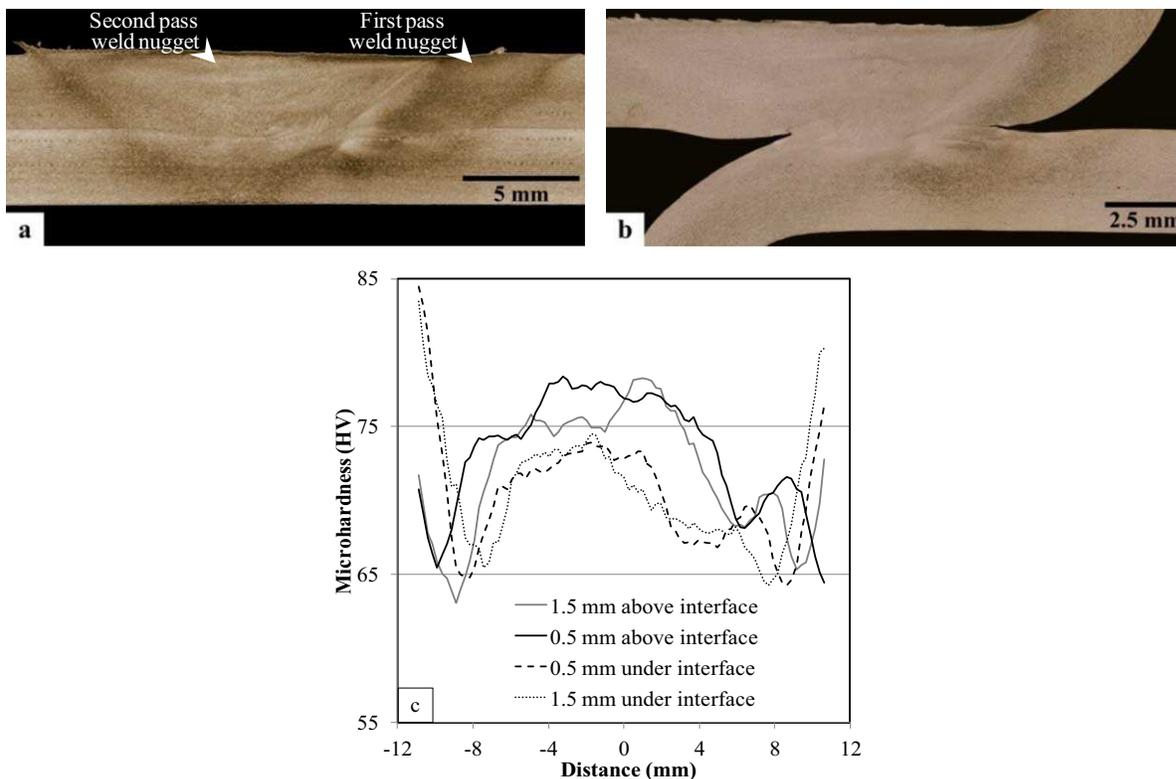

Figure 6. Friction-stir lap welded AA6061-T6 performed at a weld pitch of 0.27 mm/rev. Macrostructure (a); bend testing (b); microhardness distributions above and below the sheet interface (c).

Robotic FSW industrialization

Through an understanding of the parametric operational window, including the force requirements for FSW of butt- and lap-joint configurations in AA6061-T6, robotic scenarios can be generated to consider the industrial application of manufacturing integrated structural components with skin-to-skin and stringer-to-skin joints. **Figure 8** shows a diagrammatic representation of a structural component considered for generating the robotic scenarios; the integrated structure involves several narrow panels running along the length of the component that were assembled by means of skin-to-skin joints and a set of stringers assembled to the panels by means of stringer-to-skin joints. The
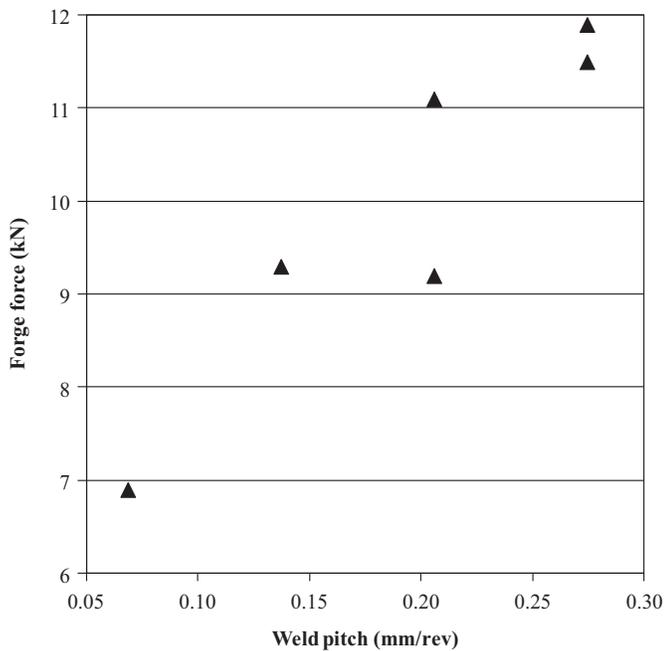

Figure 7. Forge force variation with increasing weld pitch for friction-stir lap welding of AA6061-T6.
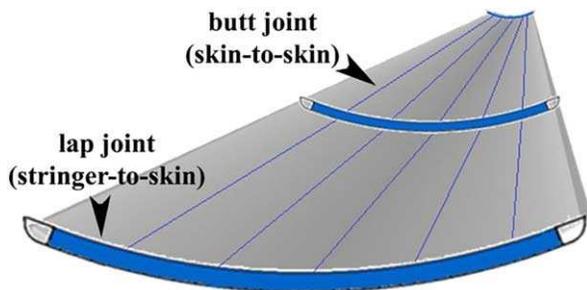

Figure 8. Perspective schematic of the large integrated structural component with stringer-to-skin and skin-to-skin joints used as the test case for this study.

findings from the process development and optimization trials as discussed in the previous sections and summarized in **Table 1**, show that the industrialization of the FSW process using serial industrial robots can be considered by evaluating different workcell layouts for manufacturing the integrated structure presented in **Figure 8**. In this paper, this analysis is considered using a KUKA KR500 MT industrial robot and a commercial-off-the-shelf (COTS) Friction Stir Link (FSL) RoboStir process end-effector, which represent the current integrated robotic FSW (RFSW) system at National Research Council Canada (NRC).

Two main types of technological limitations exist when considering serial industrial robots to industrialize FSW applications. The first limitation relates to the elastostatic and dynamic phenomena induced during the process by the high degree of elasticity of the robot joints that have been successfully compensated through a NRC proprietary control toolbox. The second limitation pertains to the non-homogeneous force capability of serial industrial robots throughout their work envelope due to the coupling of the joint configurations when generating a desired Cartesian motion. The latter is the determining factor for the design of RFSW scenarios using an industrial robot and, as such, is the main design criterion in the next subsections.

Premises for kinetostatic analysis

Considering the trajectories required for manufacturing the structural component, the resulting subspaces of the robot configurations for the butt joints are very similar to those for the lap joints as the robot system can incorporate a linear axis to accommodate the length of the component. This then allows the industrial robot to follow the "theoretical" path along each of the butt joints without changing its nominal configuration. Hence, only local changes of configurations will be necessary to accommodate inaccuracies between the real location of the FSW fixture and the elastically deformed robot using proper kinematic calibration transformation matrices and real-time path correction algorithms.

On the basis of the recommended optimal FSW operational conditions, the amplitude of the process forces was measured (**Table 1**) and determined to be typically 50% higher in the case of the lap joints compared with the butt-joint configuration. It is noteworthy that in **Table 1**, the force component, Fz (forge), is perpendicular to the workpiece surface at the weld location; Fx (drag) is in the welding direction; and Fy is perpendicular to the welding direction in the seam plane. Consequently, the main criterion for the design of RFSW scenarios thus reduces to the ability of the robotic system to develop the forces that are required for a lap-joint configuration throughout the component surface. Hence, considering a 15% contingency on all forces, the Cartesian forces that the robot needs to develop (on the basis of **Table 1**) are $|Fx| = 4.5$ kN, $|Fy| = 3.1$ kN, and $|Fz| = 13.7$ kN. Addtionally, the robot will only use Cartesian configurations in a plane

Table 1. Process forces for FSW in butt and lap configurations under the recommended operational conditions.

	Optimal weld pitch, (mm/rev)	$|Fx|$, (kN)	$|Fy|$, (kN)	$|Fz|$, (kN)
Butt-weld configuration	0.48	1.7	0.8	7.7
Lap-weld configuration	0.27	3.9	2.7	11.9

passing through, or in the vicinity of, its vertical first axis and remaining parallel to the extruded section of the component geometry. The evaluation of the robot force capability can therefore be delimited to a 2-D analysis in this particular geometric plane, hereafter referred to as Plane P.

Design of RFSW scenarios with the structural component positioned horizontally

The selected robot–workpiece configuration(s) need(s) to guarantee full reachability of the RFSW tool throughout the welding trajectories, whilst allowing the robot to sustain the process forces identified in the previous subsection. Thus to analyze the robot force capabilities, the horizontal configuration for the structural component was first considered with the premise that this layout would involve a relatively low cost and permit an ergonomic workplace setting that would facilitate the tasks of the operator(s) during setup of the workpiece within the fixture. Inherently, the highest potential for minimizing the cost related to the workcell is the horizontal configuration of the structural component with minimal elevation.

To identify such scenarios, a module was developed using MatLAB and the pseudo-code of the algorithm that computes the robot force capability within the workspace at different elevations of the structural component is provided in **Algorithm 1**.

Several configurations with full kinematic reachability over the component surface were generated using **Algorithm 1**,

which considers different elevations. **Figure 9** presents the results of the robot force capability analyses at incremental X distances from the robot base to the origin of the structural component. These results are illustrated for three elevations of the component inside the robot workspace, namely $Z = 0$ mm (**Figures 9a** and **9b**), $Z = 500$ mm (**Figures 9c** and **9d**), and $Z = 1000$ mm (**Figures 9e** and **9f**). It is noteworthy that the Y distance remains at 0 mm in this evaluation as explained earlier (2-D analysis). Although it appears that the elevation of the workpiece allows increasing the force capability of the robot along the welding trajectories, it is associated with creating interferences between the link #2 casting and the structural component (**Figure 9f**). Moreover, it is also clear from these plots that the 13.7 kN threshold for the forge force cannot be met with any of the horizontal configurations studied, thus excluding these robotic scenarios for RFSW of the structural component despite the potential for favorable costs and ergonomics. Alternative configurations were investigated through an iterative process to identify viable solutions for the workcell layout; those related to the rotation of the structural component are presented in the next subsection.

Design of workcell layouts with the structural component rotated relative to the robot

The influence of rotating the structural component with respect to the robot base on the robot force capability was investigated with, of course, the premise that the selected robot–workpiece configuration(s) need(s) to guarantee full

```
Algorithm 1

    Define 2D parametric path along structural component geometry in plane P
    and define robot associated kinematics
    FOR incremental part elevations DO
        FOR incremental distances from robot base to origin of part frame DO
            IF complete path along component section is reachable DO
                Perform kinetostatic analysis of forge force capability
                (i.e., determine the maximal force the robot is capable of developing
                in the z-direction normal to the component surface)
                Perform kinetostatic analysis of remaining drag force capability
                (determine the maximal force the robot is capable of developing in the
                welding x-direction)
                Print force capability curve for forge and drag
            ENDDO
        ENDDO
        Print force capability graph
    ENDDO
```
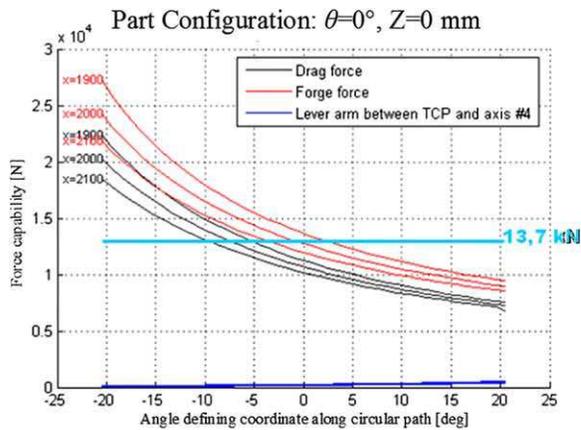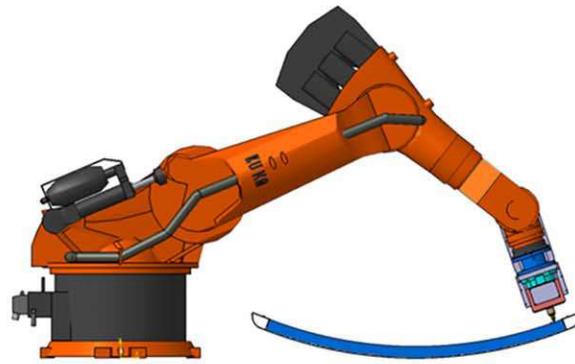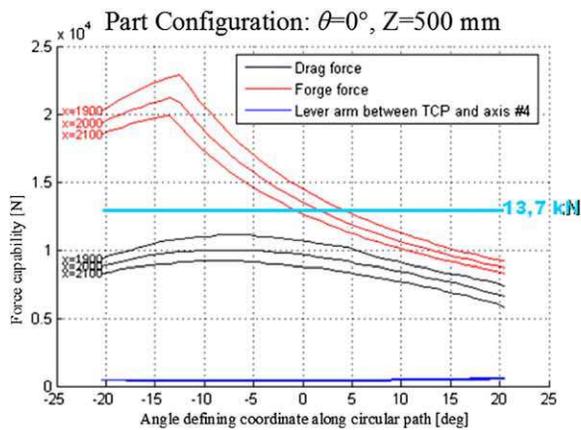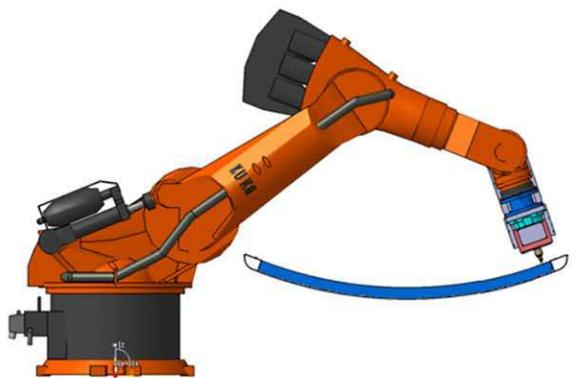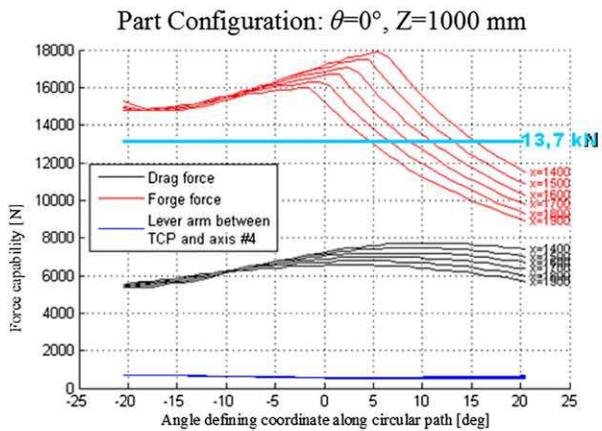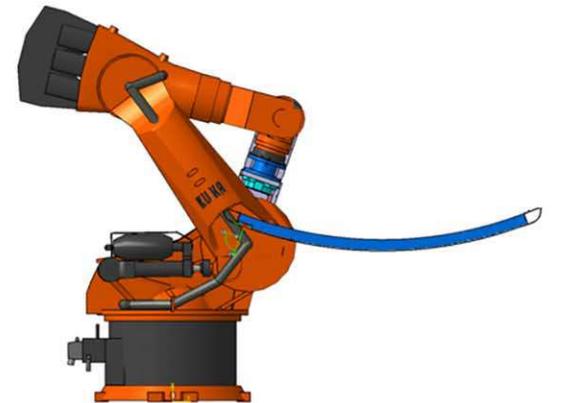
Figure 9. Analysis of the robot force capability performed for the process conditions of a double-pass lap weld with $F_y = 3.1$ kN. Force capability plots for the KR500 MT industrial robot with a FSL end-effector along the surface of a horizontal structural component in Plane $Y = 0$ mm for different elevations (Z) and increasing distances between the robot base and workpiece (X) (a, c, e). Generated robot–workpiece configurations allowing maximum robot force capability at a given elevation (b, d, f).

reachability of the RFSW tool throughout the welding paths, while allowing the robot to sustain the process forces. It is noteworthy that the rotated structural component should provide configurations with a reduced lever arm

between the forge axis and robot motors 2 and 3, thus reducing the torque required to sustain the process forces. The counter effect of rotating the component is obviously greater complexity, higher fixture-related costs and non-

optimal ergonomics for the operator performing the setup. To evaluate the evolution of the robot force capability with increasing rotation of the structural component, a variant of

Algorithm 1 was developed and employed; the variant differs from the original algorithm in that incrementation of orientation replaces incrementation of elevation.
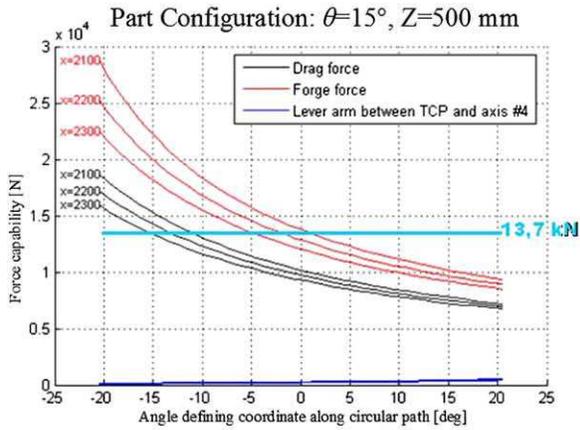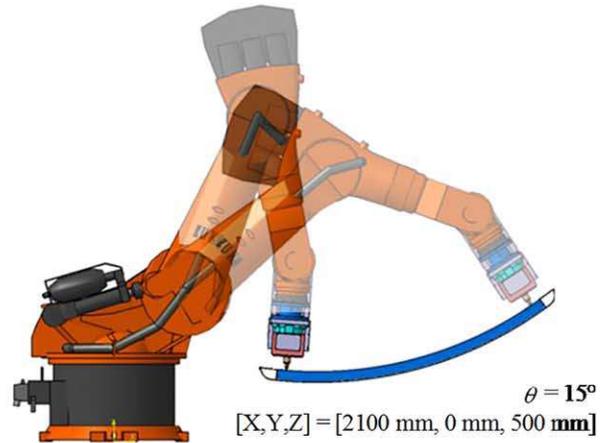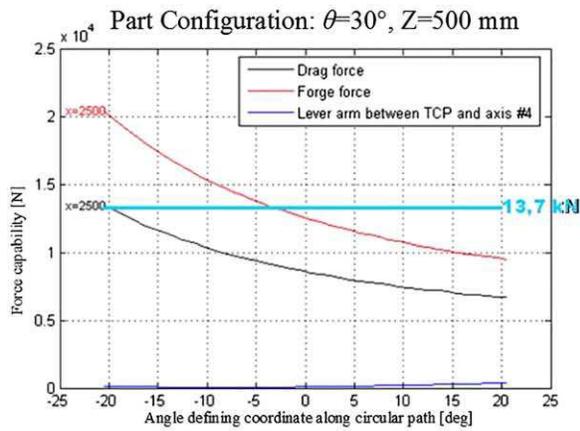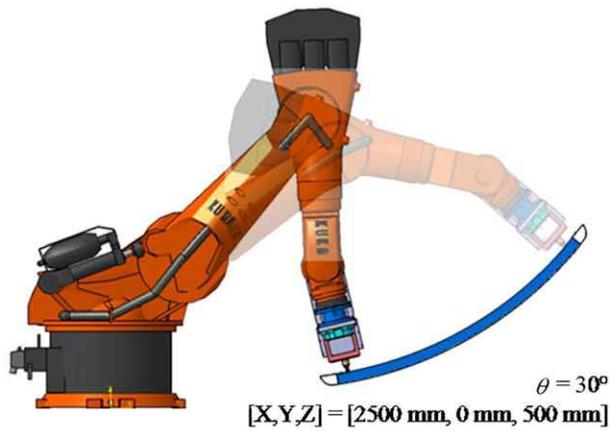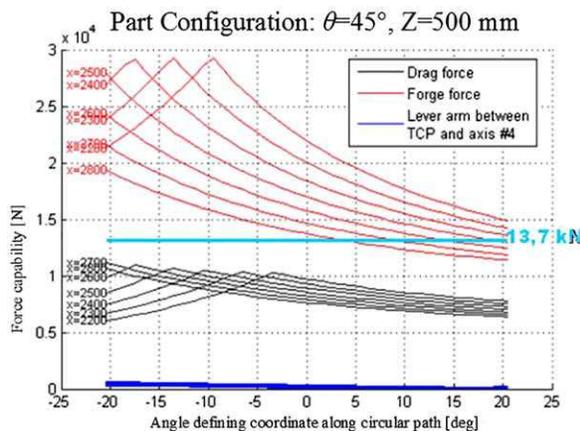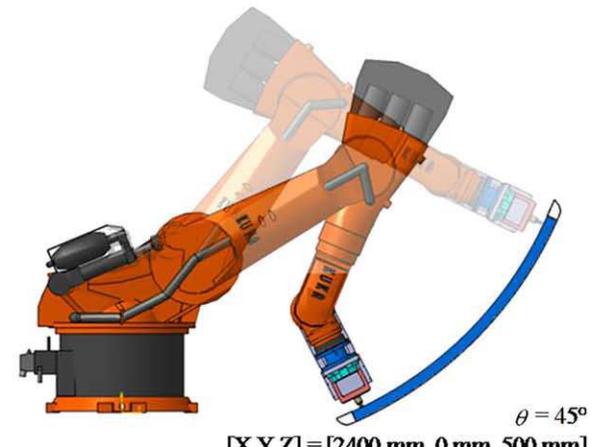

Figure 10. Analysis of the robot force capability performed for the process conditions of a double pass lap weld with $F_y = 3.1$ kN. Force capability plots for the KR500 MT industrial robot with a FSL end-effector along the surface of a structural component in Plane $Y = 0$ mm for different rotations (θ) and increasing distances between the robot base and workpiece (X) (a, c, e). Generated robot/workpiece configurations allowing maximum robot force capability at a given rotation (b, d, f).

Figure 10 presents representative results for configurations that have full kinematic reachability over the surface of the component oriented at different nominal angles (θ) and X distances from the robot base to the origin of the structural component. As before, the Y distance remains 0 mm in this evaluation. It can be presumed that the configuration with the orientation of the component corresponding to $\theta = 15°$ (**Figures 10a** and **10b**) allows for the lowest complexity and fixturing cost. However, as indicated in **Figures 10a** and **10c**, the 13.7 kN threshold for the forge force cannot be met for any of the configurations generated with an orientation of 15° or 30°. In the case of a 45° orientation between the robot and structural component (**Figures 10e** and **10f**), a viable RFSW process window is available when X ranges from 2200 mm to 2400 mm. Considering that a configuration with a maximal distance between the structure of the linear motion system supporting the robot and the workpiece will provide a better access to the operator for setup of fixtures, the configuration $X = 2400$ mm would most likely be preferable, especially since it is also exempt from kinematic singularities, which was not the case for some other configurations.

To this end, the analysis conducted and demonstrated in the present work to secure the robotic solution for the friction welding process conditions is critical to the strategy for industrialization. In effect, identifying the conditions under which the robotic operational window is compatible with the process conditions, can then allow a digital mock-up of potential workcell layouts that can be employed for budgetary estimation of the costs and the return on investment. More importantly, however, the methodology proposed in the present work can mitigate the risks associated with procuring and implementing a RFSW workcell. Without this, the workcell may prove to be non-viable for the targeted application(s).

Conclusions

For the manufacture of integrated structural components with stringer-to-skin and skin-to-skin joints, the feasibility of robotic FSW was investigated. Specifically, FSW for joining 3.18 mm thick AA6061-T6 was studied for two joint configurations, lap and butt, by considering different parametric conditions. Within the process window for each joint configuration, optimal FSW process conditions were identified. For the butt-weld configuration, zigzag oxide traces were present at the optimal weld pitch value of 0.48 mm/rev that was selected. For the lap-weld configuration at the optimal weld pitch of 0.27 mm/rev that was selected, slight thinning of the lower sheet was noticed, whereas the double oxide layer at the sheet interface was completely broken in the overlap area between the weld nuggets of the two welding passes. However, for both the butt and lap configurations, these microstructural anomalies were not observed to affect the bend performance of the joints.

To deliberate on the assembly of a structural component with RFSW, robotic scenarios were developed for a KUKA KR500 MT industrial robot and a Friction Stir Link (FSL) RoboStir end-effector. A methodology to ensure that the robotic operational window is compatible with the process conditions is presented, using the non-homogeneous force capability of the serial industrial robot throughout its work envelope. It was ascertained that the 13.7 kN threshold for the forge force could not be met with any of the horizontal fixture configurations deliberated, whereas a family of configurations with an orientation of 45° was determined as a viable robotic solution for FSW of the structural component studied in this work.

Current NRC work pertains to the development of a software capability to generate optimized robotic FSW scenarios. In particular, the software considers a general 3-D case with both optimized component position/orientation in space as well as optimized welding directions along the selected set of FSW seams. As such, once implemented, applications can be extended to the assembly of large double curvature transportation structures by means of robotic FSW. Significant effort is also dedicated to adding robustness to the friction stir welding applications by integrating tool wear, process tolerance to joint gap, tool alignment relative to the joint, and thickness mismatch.

Acknowledgements

References

American Welding Society – Technical Committee D17. 2010. Specification for Friction Stir Welding of Aluminum Alloys for Aerospace Applications, AWS D17.3/D17.3M:2010, 56 pages.

ASTM International – Subcommittee E04.05. 2011. Standard Test Method for Knoop and Vickers Hardness of Materials, ASTM E384 – 11e1, 43 pages.

Canadian Standards Association (CSA). 2011. Certification of Companies for Fusion Welding of Aluminum, CSA W47.2–11, 130 pages.

Cederqvist, L., and Reynolds, A.P. 2000. Properties of Friction Stir Welded Aluminum Lap Joints. *Proceedings of the 2nd International Symposium on Friction Stir Welding*, Gothenburg, Sweden, 9 pages.

Colegrove, P.A., Shercliff, H.R., and Hyoe, T. 2004. Development of the Trivex™ Friction Stir Welding Tool for Making Lap Welds. *5th International Symposium on Friction Stir Welding*, Metz, France, The Welding Institute, 19 pages.

Crawford, R., Cook, G.E., Strauss, A.M., Hartman, D.A., and Stremler, M.A. 2006. Experimental Defect Analysis and Force Prediction Simulation of High Weld Pitch Friction Stir Welding. *Science and Technology of Welding and Joining*, Vol. 11, No. 6, pp. 657–665. doi: 10.1179/174329306X147742.

Dubourg, L., Merati, A., and Jahazi, M. 2010. Process Optimisation and Mechanical Properties of Friction Stir Lap Welds of 7075-T6 Stringers on 2024-T3 Skin. *Materials and Design*, Vol. 31, pp. 3324–3330. doi: 10.1016/j.matdes.2010.02.002.

Fersini, D., and Pirondi, A. 2008. Analysis and Modelling of Fatigue Failure of Friction Stir Welded Aluminum Alloy Single-lap Joints. *Engineering Fracture Mechanics*, Vol. 75, pp. 790–803. doi: 10.1016/j.engfracmech.2007.04.013.

Fratini, L., Pasta, S., and Reynolds, A.P. 2008. Fatigue Crack Growth in 2024-T351 Friction Stir Welded Joints: Longitudinal Residual Stress and Microstructural Effects. *International Journal of Fatigue*, Vol. 31, No. 3, pp. 495–500. doi: 10.1016/j.ijfatigue.2008.05.004.

Indira Rani, M., Marpu, R.N., and Kumar, A.C.S. 2011. A Study of Process Parameters of Friction Stir Welded AA 6061 Aluminum Alloy in O and T6 Conditions. *Journal of Engineering and Applied Sciences*, Vol. 6, No. 2, pp. 61–66.

International Organization for Standardization – Committee TC 44/SC 10. 2004. Welding – Recommendations for Welding of Metallic Materials – Part 7: Electron Beam Welding, ISO/TR 17671-7:2004, 34 pages.

Khalid Rafi, H., Janaki Ram, G.D., Phanikumar, G., and Prasad Rao, K. 2010. Microstructure and Tensile Properties of Friction Welded Aluminum Alloy AA7075-T6. *Materials and Design*, Vol. 31, pp. 2375–2380. doi: 10.1016/j.matdes.2009.11.065.

Liu, G., Murr, L.E., Niou, C.S., McClure, J.C., and Vega, F.R. 1997. Microstructural Aspects of the Friction-stir Welding of 6061-T6 Aluminum Alloy. *Scripta Materialia*, Vol. 37, pp. 355–361. doi: 10.1016/S1359-6462(97)00093-6.

Mahoney, M.W. 2007. Mechanical Properties of Friction Stir Welded Aluminum Alloys. In: Mishra, R.S., Mahoney, M.W., (Eds.), *Friction Stir Welding and Processing*. ASM International, Materials Park, OH, USA, pp. 71–110.

Mishra, R.S., and Ma, Z.Y. 2005. Friction Stir Welding and Processing. *Materials Science and Engineering R*, Vol. 50, pp. 1–78.

Monsarrat, B., Dubourg, L., Fortin, Y., Bres, A., Guérin, M., Banu, M., Perron, C., and Wanjara, P. 2009. Friction Stir Welding of Aerospace Structures Using Low-cost Serial Industrial Robots. *European Conference on Materials and Structures in Aerospace*, Augsburg, Germany.

Moreira, P.M.G.P., Santos, T., Tavares, S.M.O., Richter-Trummer, V., Vilac, A.P., and de Castro, P.M.S.T. 2009. Mechanical and Metallurgical Characterization of Friction Stir Welding Joints of AA6061-T6 with AA6082-T6. *Materials and Design*, Vol. 30, pp. 180–187. doi: 10.1016/j.matdes.2008.04.042.

Okamura, H., Aota, K., Sakamoto, M., Ezumi, M., and Ikeuchi, K. 2002. Behaviour of Oxides during Friction Stir Welding of Aluminum Alloy and Their Effect on Its Mechanical Properties. *Welding International*, Vol. 16, No. 4, pp. 266–275. doi: 10.1080/09507110209549530.

Reddy, G.M., Mastanaiah, P., Prasad, K.S., and Mohandas, T. 2009. Microstructure and Mechanical Property Correlations in AA6061 Aluminum Alloy Friction Stir Welds. *Transactions of Indian Institute of Metals*, Vol. 62, pp. 49–58. doi: 10.1007/s12666-009-0007-z.

Scialpi, A., Thomas, W., De Filippis, L.A.C., and Staines, D.G. 2006. Staggered Twin-stir™ – Lap Joining of Aluminium Alloy. *International Journal for the Joining of Materials*, Vol. 18, No. 3/4, pp. 69–75.

Smith, C., and Hinrichs, J. 2006. Development and Qualification of a Production Capable FSW Process for 25 mm Deep Robotic Friction Stir Welds. *Proceedings of the 6th International Symposium on Friction Stir Welding*, Saint-Sauveur, Canada, 12 pages.

Soron, M., and Kalaykov, I. 2006. A Robot Prototype for Friction Stir Welding. *Proceedings of the 2006 IEEE Conference on Robotics, Automation and Mechatronics*, Bangkok, Thailand, pp. 1–5.

Thomas, W.M., and Dolby, R.E. 2002. Friction Stir Welding Developments. *Proceedings of the 6th International Conference on Trends in Welding Research*, Pine Mountain, GA, ASM International, pp. 203–211.

Thomas, W.M., Nicholas, E.D., Needham, J.C., Murch, M.G., Templesmith, P., and Dawes, C.J. 1991. "Friction Stir Butt Welding". International Patent Application No.PCT/GB92/02203 and GB patent application No.9125978.8, 6 December 1991.

Threadgill, P.L., Leonard, A.J., Shercliff, H.R., and Withers, P.J. 2009. Friction Stir Welding of Aluminium Alloys. *International Materials Reviews*, Vol. 54, No. 2, pp. 49–93.

Voellner, G., Zaeh, M.F., Kellenberger, O., Lohwasser, D., and Silvanus, J. 2006. 3-Dimensional Friction Stir Welding Using a Modified High Payload Robot. *Proceedings of the 6th International Symposium on Friction Stir Welding*, Saint-Sauveur, Canada, 12 pages.

Wanjara, P., Monsarrat, B., and Larose, S. 2013. Gap Tolerance Allowance and Robotic Operational Window for Friction Stir Butt Welding of AA6061. *Journal of Materials Processing Technology*, Vol. 213, pp. 631–640. doi: 10.1016/j.jmatprotec.2012.10.010.

Zhang, Y.M., Pan, C., and Male, A.T. 2000. Improved Microstructure and Properties of 6061 Aluminum Alloy Weldments Using a Double-sided Arc Welding Process. *Metallurgical and Materials Transactions A*, Vol. 31, No. 10, pp. 2537–2543. doi: 10.1007/s11661-000-0198-8.

Zimmer, S., and Laye, J. 2009. Robotized Friction Stir Welding. *International Workshop on Friction Stir Welding*, Sophia Antipolis, France.